Research in Astronomy and Astrophysics, 23:015023 (11pp), 2023 January https://doi.org/10.1088/1674-4527/aca8ee

Research on a Coherent Dedispersion Algorithm for Pulsar Baseband Data

Hai-Long Zhang[1,2,3,4], Ya-Zhou Zhang[1,2], Meng Zhang[1,2], Jie Wang[1,4], Ting Zhang[5], Shuang-Qiang Wang[1], Jian-ping Yuan[1], Xin-Chen Ye[1,2,4], and Jian Li[1]

[1] Xinjiang Astronomical Observatory, Chinese Academy of Sciences, Urumqi 830011, China; zhanghailong@xao.ac.cn
[2] University of Chinese Academy of Sciences, Beijing 100049, China
[3] Key Laboratory of Radio Astronomy, Chinese Academy of Sciences, Nanjing 210008, China
[4] National Astronomical Data Center, Beijing 100101, China
[5] College of Physics and Astronomy, China West Normal University, Nanchong 637002, China
Received 2022 September 15; revised 2022 November 27; accepted 2022 December 4; published 2023 January 11

Abstract

When the pulsar signal propagates in the interstellar medium (ISM), the high frequency and low frequency components of the signal reach the radio telescope with a certain delay. Therefore, the pulsar signal will appear energy dispersion, which will broaden the pulse profile, decrease the signal to noise ratio, and even lead to the disappearance of the pulse signal. In this paper, we analyze the sampling, polarization and arrangement of baseband data based on the coherent dedispersion algorithm for the problem of pulsar baseband data dedispersion. We systematically study the coherent dedispersion data processing procedure, and test the pulse profile changes under different FFT block sizes. An optimal selection strategy of FFT block sizes is proposed for reducing the operation time and obtaining a better pulse profile. We propose two methods, one is the generation of ISM transfer function, the other is the pulsar period and phase prediction method at a certain time, and discuss integral and folding strategies. We test the algorithm based on the baseband data of CASPSR and Medusa terminals observed by the Parkes 64 m radio telescope, and analyze the reading and processing methods of baseband data of different terminals. The experimental results show that the phase and amplitude information of the pulse profile processed by our algorithm is basically consistent with the results obtained by DSPSR.

Key words: pulsar: – coherent dedispersion: – baseband data: – pulse profile

1. Introduction

A pulsar[6] is a highly magnetized rotating neutron star that emits beams of electromagnetic radiation out of its magnetic poles. This radiation can be observed by radio telescopes only when a beam of emission is pointing toward the Earth (Lorimer & Kramer 2012). Because of their special physical properties, pulsars can provide astronomers with a physical environment, which cannot be simulated on the Earth, and a lot of important data for basic physics research. As the pulsar emission propagates through space, its signal is affected by interstellar medium (ISM). The latter causes the pulse profile to broaden and deform, and the high-frequency signal will reach the Earth before the low-frequency signal. The phenomenon is called dispersion. At present, there are two kinds of dedispersion techniques used in pulsar data processing: incoherent dedispersion (Liu et al. 2022) and coherent dedispersion (Luo et al. 2017). Incoherent dedispersion algorithm realizes channel division through filter banks, and then calculates the delay in each sub-channel separately. According to the delay for each sub-channel, the data can be aligned to remove the dispersion. The dispersion effect cannot be completely eliminated by the incoherent desorption algorithm because there are corresponding high frequency parts and low frequency parts inside each subband. Moreover, the subband division cannot be infinitely small, so the dispersion effect in the subband cannot be removed by the incoherent dispersion algorithm. For precision observation, incoherent dedispersion technology cannot meet the accuracy requirement (Kong et al. 2021).

In 1975, Rickett (1975) proposed a pulsar coherent dispersion algorithm. According to Rickett, the dispersive effect of ISM is equivalent to that of a filter with a correlated transfer function. Therefore, the reciprocal of the transfer function can be used as a "filter" to filter the received pulsar signal, which can completely eliminate the dispersion effect theoretically. However, the coherent dedispersion algorithm was not widely used, because the computer performance at that time could not meet the computational requirements. With the rapid development of modern computer technology and the urgent need of scientific research, the coherent dedispersion technology has gradually become the mainstream now.

At present the most famous open source software of coherent dedispersion is DSPSR (van Straten & Bailes 2011), which has become a widely used pulsar data processing

[6] https://en.wikipedia.org/wiki/Pulsar

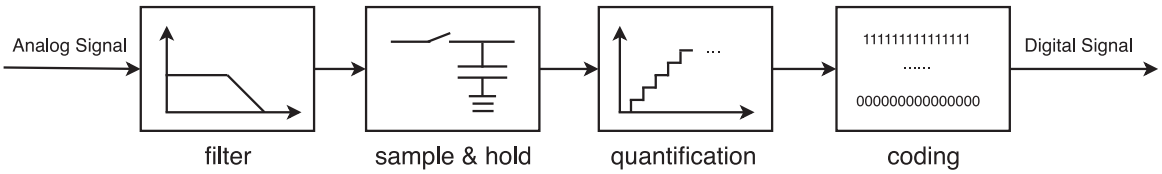

Figure 1. ADC Process Structure.

software for astronomers and researchers. However, in order to cope with the various astronomical data formats and various complex functional requirements, the dependence relationship between DSPSR and other pulsar data processing software has increased in complexity, which is not easy for beginners to analyze and research.

In this paper, the process of pulsar coherent dedispersion is analyzed in detail. The coherent dedispersion algorithm is designed and implemented, and the implementation details of the algorithm and the corresponding precautions are discussed. The baseband data recorded by CASPSR (Hickish et al. 2016; Naldi et al. 2017) and Medusa (Hobbs et al. 2020) backends are used to test the algorithm, and the effectiveness of the algorithm is verified.

2. PSRDADA Baseband Data Format

The original analog voltage signal obtained by the radio telescope receiver will be quantified into digital signal by the ADC (analog-to-digital converter), and the quantized digital signal can be called baseband data.

2.1. ADC sampling

ADC is used in radio astronomy to convert time continuous and amplitude continuous analog signals into time-discrete and amplitude discrete digital signals (Ergesh et al. 2022). The conversion of analog signals to digital signals generally is processed through sampling, holding, quantization and coding (Li 2015). The ADC sampling process is shown in Figure 1.

The two main performance indicators of ADC are resolution and sampling rate. The resolution of an ADC refers to the minimum change of the value it can represent. For an ideal ADC, the transfer function is a ladder with step width equal to the resolution. Since the output of the ADC is a discrete digital signal and the input is a continuously varying analog signal, the output of the ADC is subject to quantization error. Figure 2 shows a graphical representation of the quantization error with a 3 bit ADC. In this case, V_{input}(Unit: V) is the input quantization voltage. The quantization error is within 1 LSB, and the maximum error is 1 LSB.

2.2. Polarization

Astronomy involves the reception of the electromagnetic signal from objects beyond the Earth. Light from these distant objects can arrive at a telescope with its electric field having some preferred orientation or rotation. This tendency is known as polarization (Robishaw & Heiles 2021). A polarized ware can be described using four Stokes parameters, I, Q, U and V.[7] I represents the total intensity, Q and U are the orthogonal components used to describe linear polarization with intensity $L = \sqrt{Q^2 + U^2}$ and V is the circular polarization.

Celestial bodies emit different kinds of polarized electromagnetic waves. For example, extragalactic radio sources and pulsars are mainly linearly polarized, and these sources usually have no circular polarization.[8]

Most of the radio telescope receiving systems generate two polarized signals, which are usually stored alternately in baseband data. The SNR of the signal can be increased by $\sqrt{2}$ times by processing the two channels of polarization signals simultaneously.

2.3. Baseband data format

The polarization arrangement and quantization bit number of PSRDADA[9] format baseband data recorded by CASPSR and Medusa backends at the Parkes 64 m radio telescope are different. The PSRDADA data recorded by CASPSR contains header information and data information. Dual-polarized data are stored in groups of four alternately, and each polarization data occupies a width of 8 bits. The storage format of CASPSR baseband data is shown in Figure 3.

The Medusa baseband data files store complex numbers (real & imaginary). Each complex sample occupies 32 bits, which is stored as 16 bits real, followed by 16 bits imaginary, and all the data are signed 16 bits integers. The baseband data are stored in heaps of 2048 time samples. Each heap is stored as 8192 bytes: 2048 complex samples from pol_A [samples 0–2047], 8192 bytes 2048 complex samples from pol pol_B [samples 0–2047] and so on, as shown in Figure 4. Note that each 16 bits value is stored in offset binary encoding, and data format conversion is required before use.[10]

[7] https://en.wikipedia.org/wiki/Stokes_parameters
[8] http://www.gmrt.ncra.tifr.res.in/doc/WEBLF/LFRA/node134.html
[9] https://sourceforge.net/projects/psrdada/
[10] The data format interpretation is from Andrew Jameson (ajameson@swin.edu.au). Thanks for his explanation of the Medusa baseband data format.

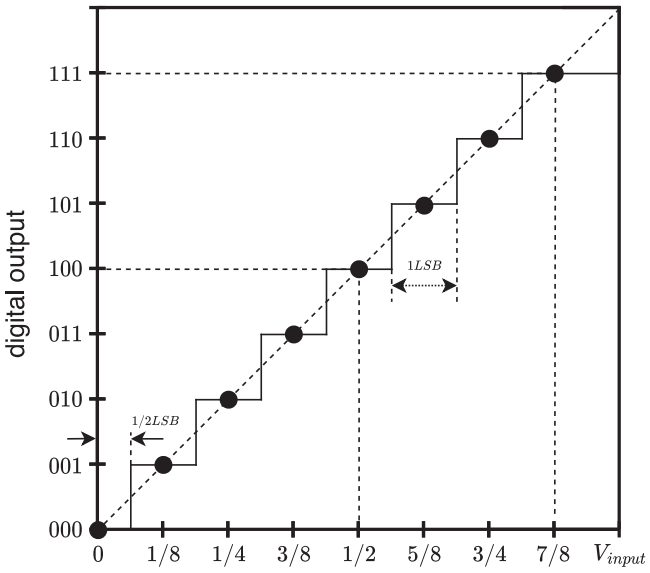

Figure 2. Quantization coding of 3 bits ADC.

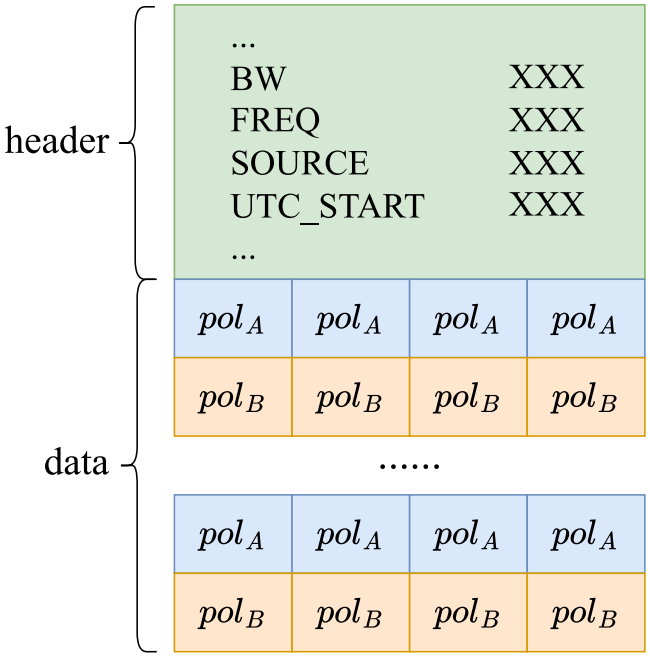

Figure 3. CASPSR baseband data arrangement.

3. Coherent Dedispersion

The coherent dedispersion operation is to convolve the original voltage data (Nyquist sampling time series) with the inverse of ISM transfer function. Based on the discrete convolution theorem, the convolution can be quickly performed in the frequency domain (Bassa et al. 2017). The key of coherent dedispersion operation is calculating ISM transfer function.

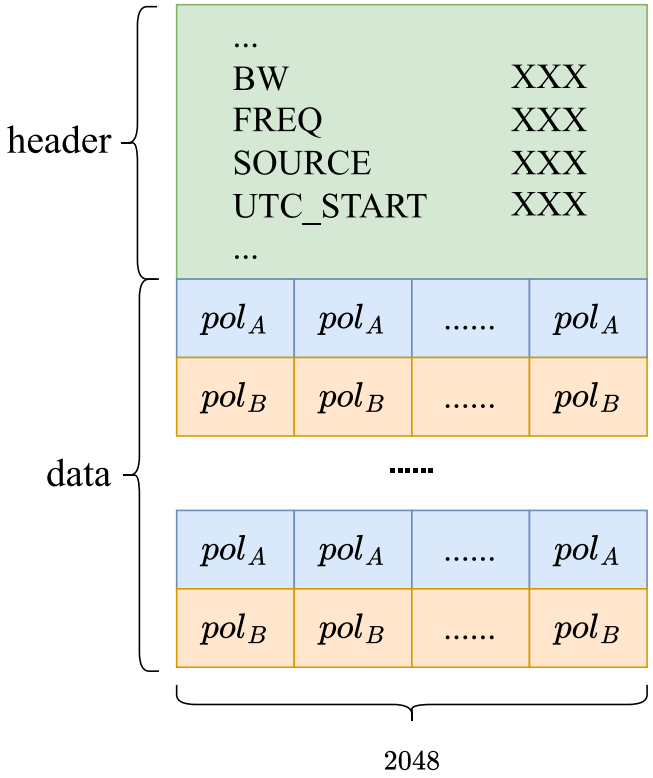

Figure 4. Medusa baseband data arrangement.

3.1. ISM Transfer Function

The dispersion effect (Hewish et al. 1968) of the ISM on radio waves is equivalent to the radio waves passing through a filter with the ISM transfer function. The dispersion effect caused by ISM can be eliminated by passing the observed signal through a filter with the reciprocal of the ISM transport function. We suppose that the pulsar propagation signal in the time domain is $v_{\rm int}(t)$, the pulsar signal voltage obtained by radio telescope observation is $v(t)$, and the response function of ISM is $h(t)$, then

$$v(t) = v_{\rm int}(t) * h(t). \quad (1)$$

Based on the convolution theorem, the convolution of a sequence in the time domain is equivalent to the product of the sequence in the frequency domain, then

$$V(f) = V_{\rm int}(f)H(f). \quad (2)$$

$V(f)$, $V_{\rm int}(f)$ and $H(f)$ are the Fourier transform results of $v(t)$, $v_{\rm int}(t)$ and $h(t)$, respectively, and $H(f)$ is the transfer function, where f is the observed frequency. We set the reference frequency $f_{\rm ref}$, the size of a certain frequency point f from $f_{\rm ref}$ as

shown in Equation (3).

$$\Delta f = f - f_{\rm ref}. \tag{3}$$

Then Equation (2) can be rewritten as

$$V(f_{\rm ref} + \Delta f) = V_{\rm int}(f_{\rm ref} + \Delta f)H(f_{\rm ref} + \Delta f). \tag{4}$$

The phase obtained for electromagnetic waves propagating in the ISM is given by Equation (5) (Lorimer & Kramer 2012).

$$\phi(f) = 2\pi f\frac{L}{c}\left(1 - \frac{f_p^2}{2f^2}\right), \tag{5}$$

where L is the distance from the Earth in the ionized plasma, f_p is the plasma frequency of ISM, c is the speed of light, and the transfer function can be written as

$$H(f_{\rm ref} + \Delta f) = e^{-i\phi(f_{\rm ref}+\Delta f)}. \tag{6}$$

Using the Taylor expansion, the first three terms of $\phi(f_{\rm ref}+\Delta f)$ can be written as

$$\phi(f_{\rm ref} + \Delta f) = 2\pi\frac{L}{c}\left[\left(f_{\rm ref} - \frac{f_p^2}{2f_{\rm ref}}\right) + \left(1 + \frac{f_p^2}{2f_{\rm ref}^2}\right)\Delta f - \left(\frac{f_p^2}{2(f_{\rm ref} + \Delta f)f_{\rm ref}^2}\right)(\Delta f)^2\right]. \tag{7}$$

The first term in the square brackets in Equation (7) is a phase offset constant, the second term is a linear frequency gradient, which corresponds to the time delay of pulse arrival, and the third term causes dispersion in the frequency band, which needs to be corrected. The transfer function of dispersion is the inverse of the third term on the right-hand side of Equation (7), which can be expressed as,

$$H(f_{\rm ref} + \Delta f) = \exp\left[2\pi\frac{L}{c}i\frac{f_p^2}{2(f_{\rm ref} + \Delta f)f_{\rm ref}^2}(\Delta f)^2\right]. \tag{8}$$

Equation (8) can be rewritten as

$$H(f_{\rm ref} + \Delta f) = \exp\left[i\frac{2\pi D}{2(f_{\rm ref} + \Delta f)f_{\rm ref}^2}DM(\Delta f)^2\right], \tag{9}$$

where D and DM are known parameters, as shown in Equations (10) and (11).

$$D \equiv \frac{e^2}{2\pi m_e C} \approx 4.15 \times 10^3 {\rm MHz}^2 \cdot pc^{-1} \cdot cm^2 \cdot s, \tag{10}$$

$$DM = \int_0^d n_e dl. \tag{11}$$

In Equations (11), n_e is the electron density in interstellar space, and l is the distance of the observed pulsar to the radio telescope. The ISM transfer function can be obtained by Equation (9) , which gives

$$H(f_{\rm ref} + \Delta f)^{-1} = \exp\left[-i\frac{2\pi D}{2(f_{\rm ref} + \Delta f)f_{\rm ref}^2}DM(\Delta f)^2\right]. \tag{12}$$

3.2. CHIRP Function

Spectrum aliasing may occur when wideband signals are filtered by physical filters at the backends of radio telescope receivers. In order to prevent the effect of spectrum aliasing on pulsar dedispersion process, the taper function can be added to suppress the edge aliasing (Stairs 1998). The product of taper function and reciprocal of transfer function is called CHRIP function (De & Gupta 2016). The CHIRP function can be expressed as follows.

$$\begin{aligned}{\rm chrip} &= {\rm taper} \cdot H^{-1} \\ &= {\rm taper} \cdot \exp\left[i\frac{\pm DM(\Delta f)^2}{(2.41 \times 10^{-10})(f_{\rm ref} + \Delta f)f_{\rm ref}^2}\right],\end{aligned} \tag{13}$$

where $f_{\rm ref}$ is the center frequency. For upper baseband data (in the header information, the bandwidth value is positive), the numerator in the fraction of Equation (13) is a negative sign; for lower baseband data (in the header information, the bandwidth value is negative), it is a positive sign. The taper function is shown in Equation (14) (Stairs 1998).

$${\rm taper} = \frac{1}{N}\left[1 + \left(\frac{f_k}{0.47B}\right)^{80}\right]^{-1/2}, \tag{14}$$

where N is the number of frequency domain points, $1/N$ is the normalization of the data after dedispersion, and B is the frequency band bandwidth. Applying the taper function, it is able to suppress the edge-aliased signal, as shown in Figure 5.

4. Pulsar Baseband Data Processing

The pulsar data processing flow is shown in Figure 6, where the data are processed in blocks. The dual-polarized data are read from the baseband data and processed separately, each polarization data needs to be transformed to the frequency domain for coherent decontamination. Then, the frequency domain data is converted to the time domain by IFFT, and the two polarization data are merged again. As shown in Equation (15), $\rm pol_A$ and $\rm pol_B$ represent the time-domain data of polarization A and polarization B. By predicting the exact period and the phase of the sampling point, the algorithm in this paper integrates and folds all the blocks to obtain the pulse profile.

$${\rm total\_intensity} = \sqrt{{\rm pol}_A^2 + {\rm pol}_B^2}. \tag{15}$$

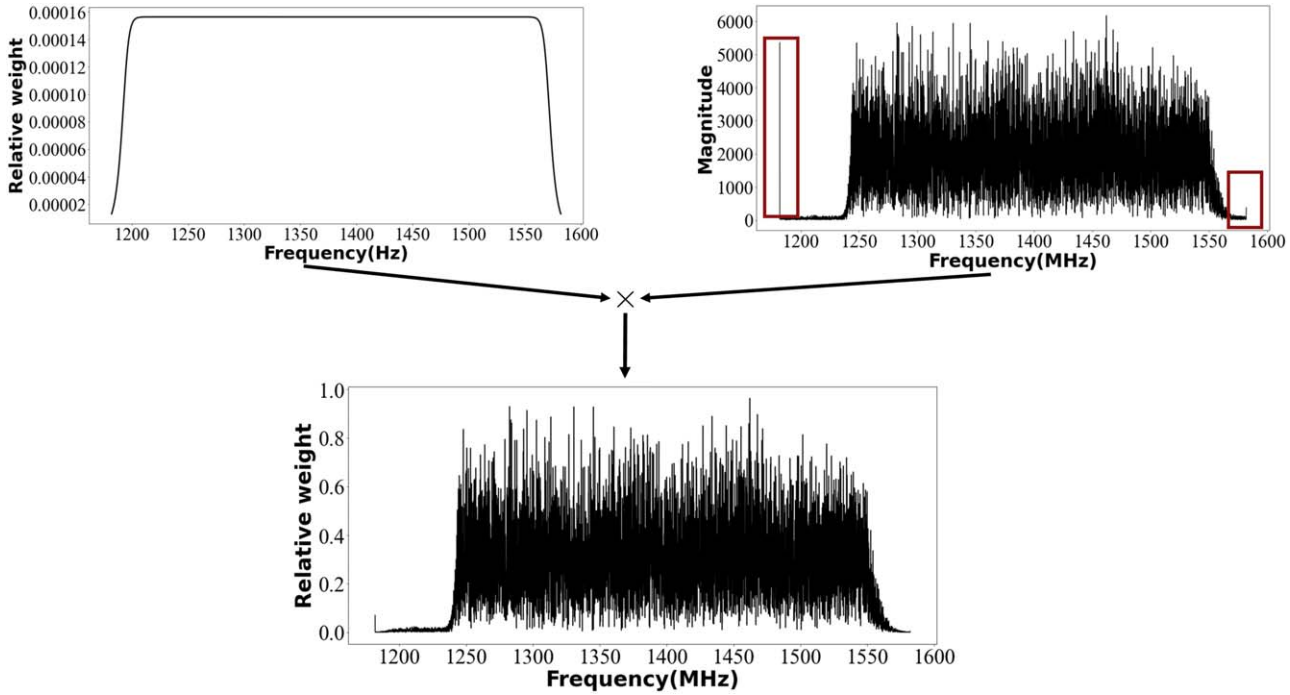

Figure 5. The taper function execution process. The image of the taper function is shown in the upper left figure, and the upper right figure is the spectrum of J0437–4715 with bandwidth of 400 MHz and the center frequency of 1382 MHz. Multiplying them both, the results are shown below, and it can be seen that the red square circled in the upper right figure, the anomalous signal caused by the spectral overlap is effectively suppressed.

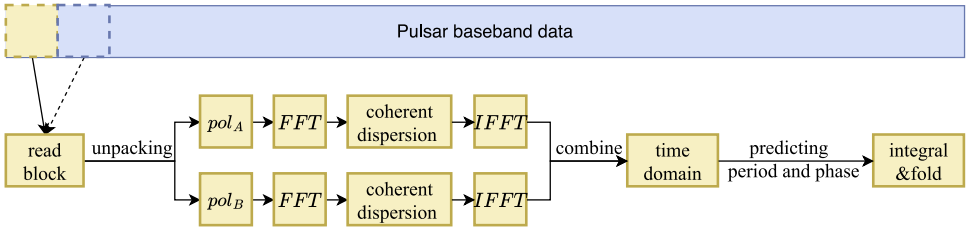

Figure 6. Pulsar baseband data processing flow.

4.1. FFT Strategy

To improve the efficiency of processing and to facilitate the prediction of pulsar folding periods and phases, pulsar baseband data need to be processed in blocks. The most time-consuming step in the processing is the coherent dedispersion, which has a time complexity of $O(n\log n)$ (FFT operations account for the majority). When performing FFT operations on periodic signals, it is necessary to select a suitable block size, and the selected length should also satisfy two basic conditions: (1) Blocks size at least greater than one pulsar period of sampling points; (2) Reduce the computation time as much as possible. The time complexity of the current fastest FFT algorithm is $O(n\log n)$. We suppose the length of the baseband data is N and the size of each block is M, then the total time complexity is shown in Equation (16).

$$T(N) = O\left(\frac{N}{M} \times M \log M\right) = O(N \log M). \tag{16}$$

From Equation (16), it can be seen that the smaller the size of each block, the smaller the overall computation time. But the size of the block is at least larger than the number of sampling points of one pulsar cycle and satisfies the power of 2 exponential size, otherwise the final pulse profile is seriously affected.

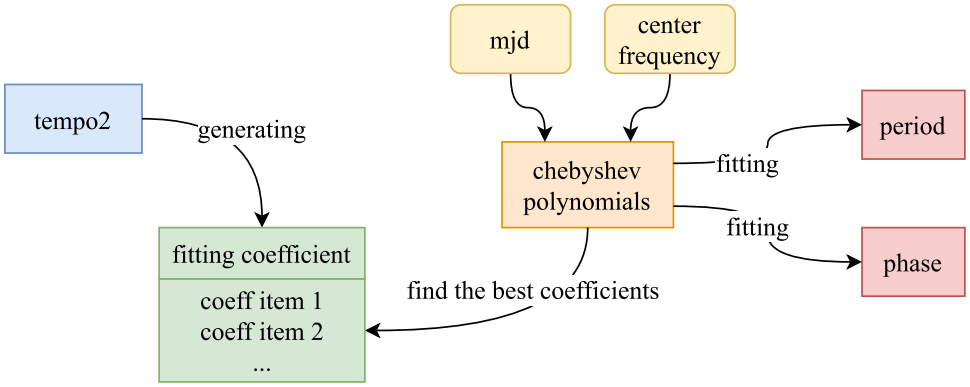

Figure 7. Folded period and phase prediction process.

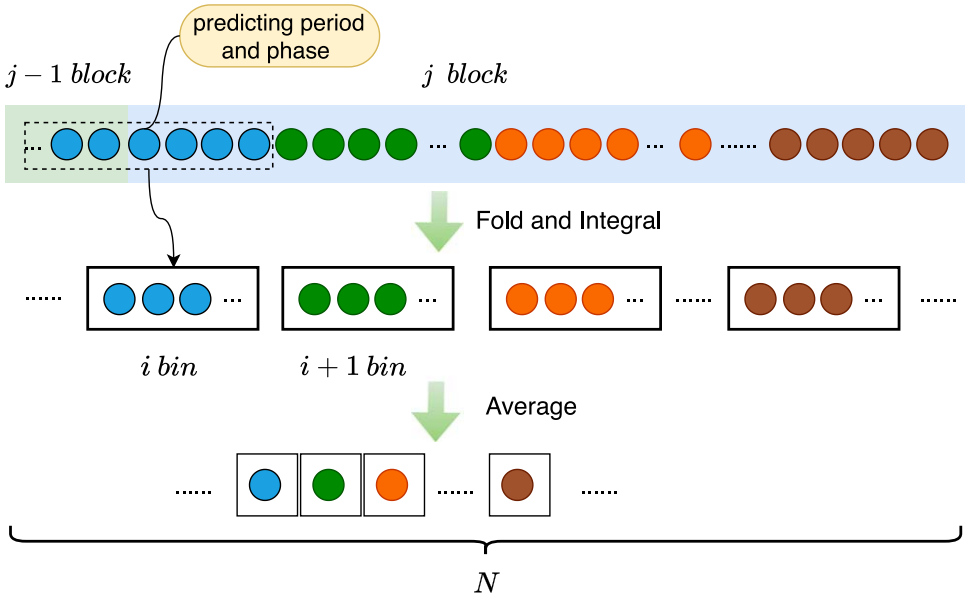

Figure 8. Pulsar baseband data folded and integrated by block. Before processing each block, the period and the phase of the first adopted point of that block need to be predicted. For example, the phase of the first sampling point of the *j*th block in the figure can be known as *i* bin by prediction, then all subsequent sampling points of that block can be solved and placed in a bin belonging to itself. Finally, the final result is obtained by averaging.

4.2. Period and Phase Prediction

The pulsar period is very stable, but the location of the observatory, the pulsar dispersion, the orbital parameters of the solar system, and the binary star system all affect the pulse arrival time (TOA) (Pennucci 2015). In order to accurately fold the pulse profile to obtain the arrival time, it is necessary to predict the pulse folding period and phase, the process is shown in Figure 7. Multiple sets of fitting coefficients are generated based on TEMPO2 (telescope, time range, frequency range and other information need to be specified), and the optimal fitting coefficients are calculated with time and center frequency as parameters. Then, the folding period and phase value are calculated by fitting the Chebyshev polynomial (Hobbs & Edwards 2012).

4.3. Fold and Integral

The final pulse profile can be obtained by folding and integrating all the blocks after the dedispersion operation is completed. In order to accurately fold the pulse profile, it is necessary to predict the pulse folding period based on the observation time and the relative phase value (between 0 and 1) of the first sampling point of each block, and then the phase values of all sampling points of the block are calculated. The

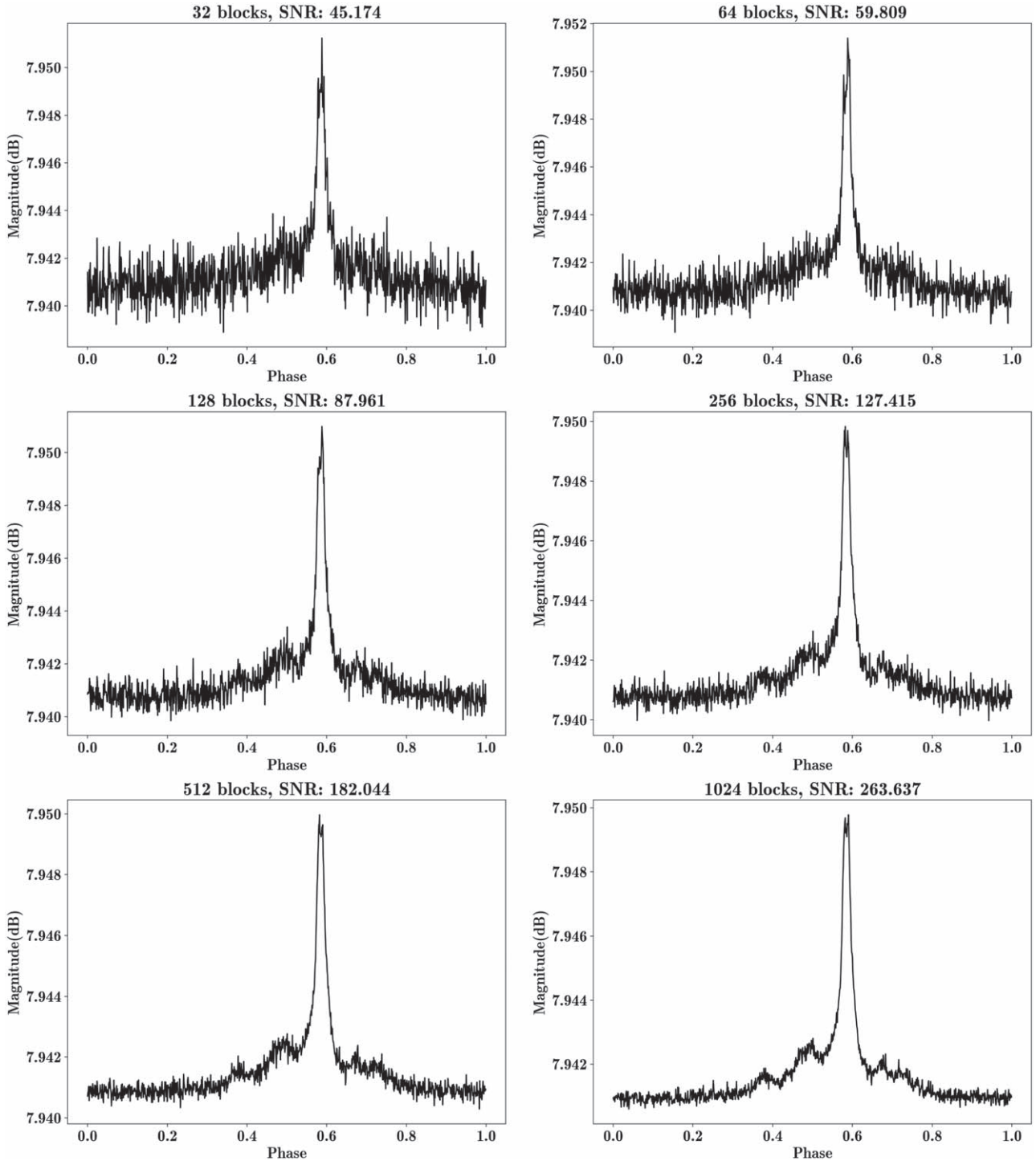

Figure 9. J0437–4715 pulse profile (1182–1582 MHz).

phase value of the *i*th sample point is shown in Equation (17).

$$\begin{aligned}\text{phase}_i &= (\text{phase}_1 + i * \text{phase\_per\_sample}) \\ &-\text{floor}(\text{phase}_1 + i * \text{phase\_per\_sample}),\end{aligned} \tag{17}$$

where phase_1 is the phase value of the 1st sampling point, predicted by the algorithm mentioned in Section 4.2, floor() function indicates rounding down, and phase_per_sample indicates the phase size interval of each sampling point as

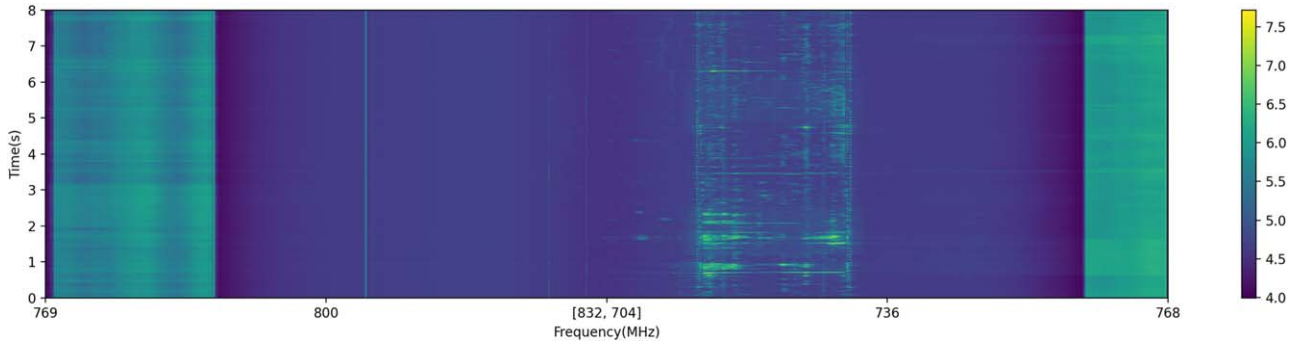

Figure 10. Medusa Baseband Data Waterfall.

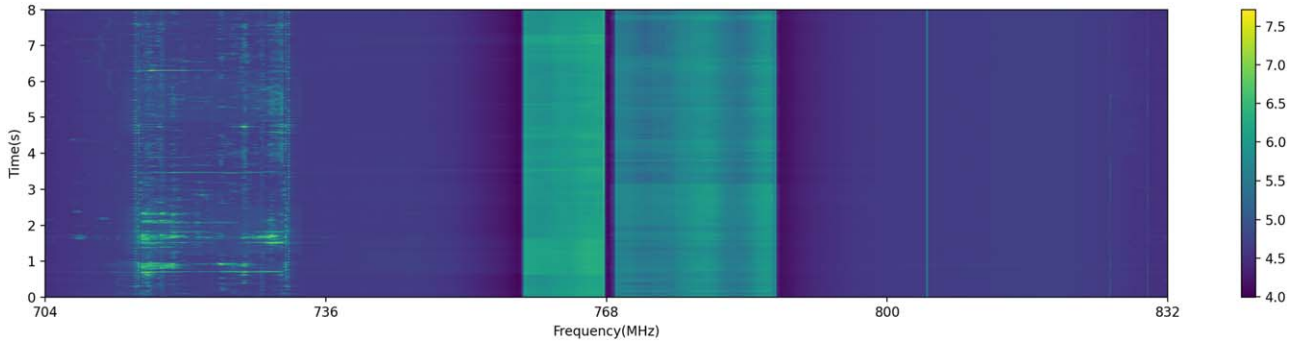

Figure 11. Waterfall of Medusa baseband data after fft_shift.

shown in Equation (18).

$$\text{phase\_per\_sample} = \frac{1}{\text{rate}} \times \frac{1}{\text{period}}, \tag{18}$$

where rate indicates the sampling rate and period is the folding period. After calculating the phase value of each sample point, each sample point can be put into the corresponding bin. Suppose there are *n*bin sample points after integration, then the *i*th sample point corresponding to the bin number is shown in Equation (19).

$$i\text{bin} = \text{phase}_i \times n\text{bin}. \tag{19}$$

As shown in Figure 8, the sampled points in each block are put into the corresponding bin, and the collapsed and integrated pulse profile is obtained by averaging the data within each bin.

5. Results

5.1. CASPSR Baseband Data Coherent Dedispersion Processing

The algorithm was tested using the baseband data generated by CASPSR backends of the Parkes 64 m radio telescope. The object name is J0437–4715, observation date is 2011 October 29-20:52:32, dual-polarized 8 bits sampling, bandwidth is 400 MHz, bandwidth range is 1182–1582 MHz, observation time is 8 s, and the data file size is 12.8 GB. As shown in Figure 9, we use different numbers of blocks for coherent dedispersion and folding, where Blocks $= 2^{22}$. It is clear that the pulsar SNR increases as the number of blocks increases.

5.2. Medusa Baseband Data Coherent Dedispersion Processing

The algorithm was systematically tested using the baseband data generated by the Medusa backends of the Parkes 64 m radio telescope, the source name is J0437–4715, the observation date is 2022 June 9-00:11:22, the observation file is dual-polarized 16bits sampling, the bandwidth size is 128 MHz, the bandwidth range is 704–832 MHz, the observation time is about 9.6 s, and the data file size is 9.6 GB. Medusa records two-sideband data, which needs to be rearranged before being converted to the frequency domain by FFT for coherent dedispersion, the first half of the spectrum should be exchanged with the second half. As shown in Figure 10, a waterfall plot of Medusa baseband data, the first half is the high-frequency spectrum, while the second half is the low-frequency part, which needs to be subjected to the fft_shift[11] operation, and the shifted result is shown in Figure 11. RFI existed in the

[11] https://www.mathworks.com/help/matlab/ref/fftshift.html

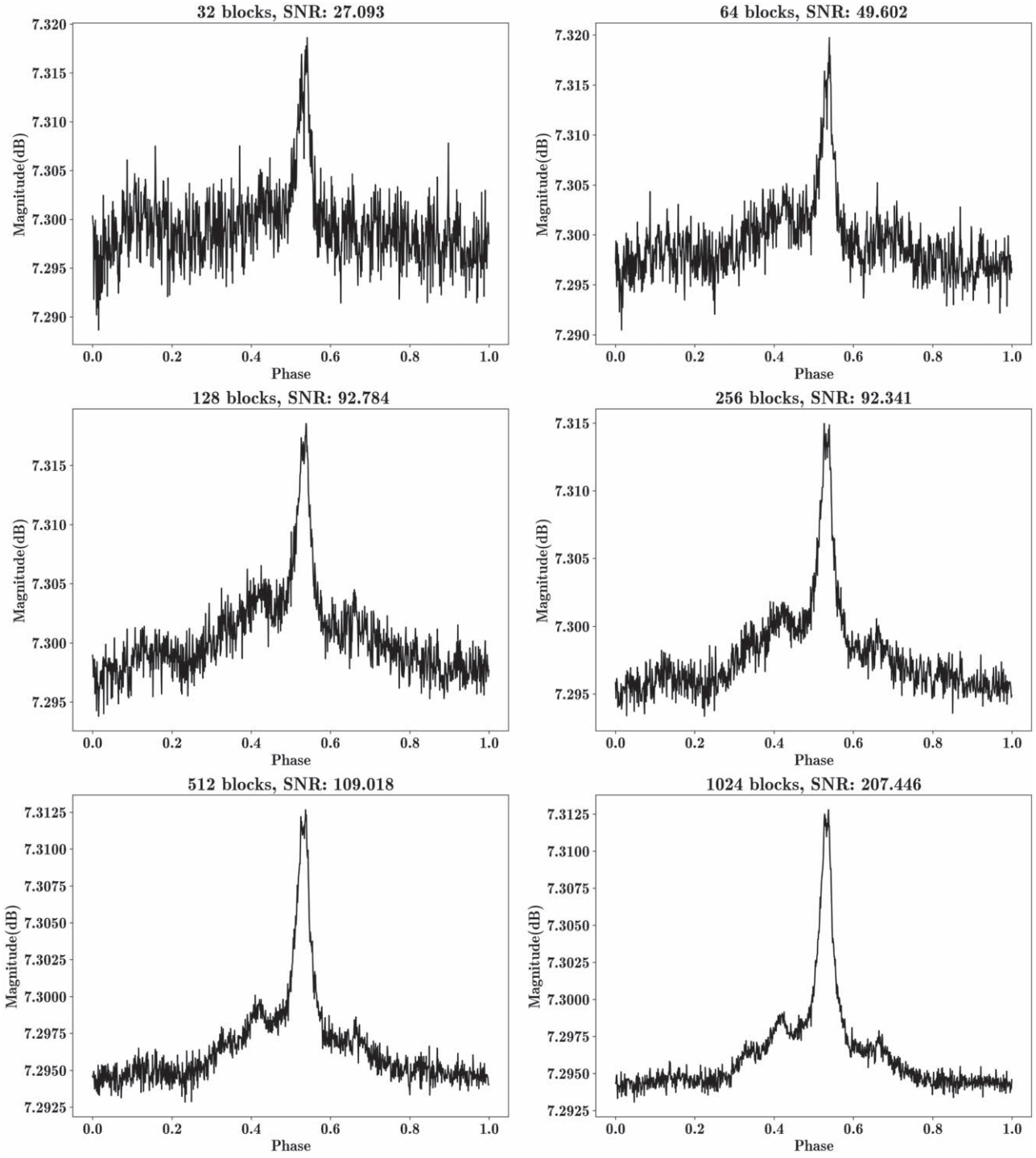

Figure 12. J0437-4715 pulse profile(810–832 MHz).

baseband data recorded by Medusa, and a relatively clean frequency band of 810–832 MHz was selected for testing, where block $= 2^{20}$. The results are shown in Figure 12.

The comparison between the predicted phase and the folded pulse profile in this paper and the processing results of DSPSR/PSRCHIVE (van Straten et al. 2012) is shown in

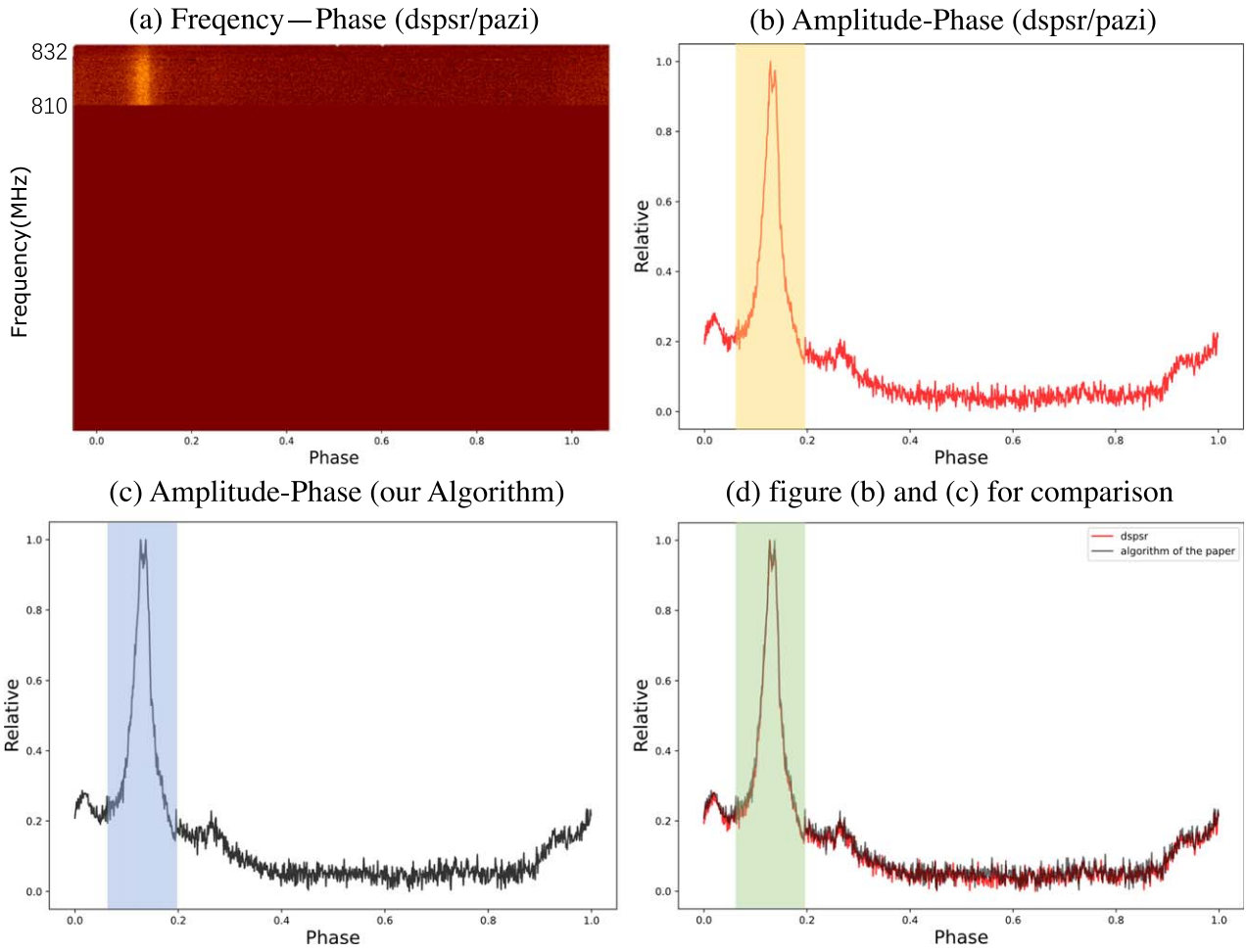

Figure 13. Comparison of the algorithm in this paper with dspsr/psrchive processing results.

Figure 13. Figure 13(a) shows that only the bandpass information of 810–832 MHz is kept, Figure 13(b) shows the process result obtained from DSPSR/PSRCHIVE, Figure 13(c) is the processing result of our algorithm and Figure 13(d) is the overlap of the two profiles. The phase and pulse profile are basically consistent, which verifies the effectiveness of the algorithm in this paper.

6. Discussion

This paper systematically analyzed the baseband data formats, dual-polarized data processing, and provided a brief overview of ADC sampling and quantization coding. A coherent dedispersion algorithm based on pulsar baseband data is designed. Aiming at the problem of FFT block size selection in algorithm design, the optimal FFT block size selection strategy is designed. Under the premise of ensuring the quality of pulse profile, the FFT block size is selected as the smallest power exponent closest to the integer multiple of the pulsar period to speed up the computation time. For the generation of CHRIP function, the taper function, application scenarios and the selection of positive and negative signs of upper and lower sideband data are analyzed. In order to predict the period and phase of pulsar at a certain time, TEMPO2 is used to generate fitting coefficients based on time and center frequency. Chebyshev polynomial and coefficients are used to fit and predict the exact period and phase of pulsar. The pulsar data folding and integration are realized based on the calculated period and phase in a block.

The algorithm was tested based on the baseband data of pulsar J0437-4715 recorded by the CASPSR backend of the Parkes 64 m radio telescope. The SNR of pulse profile was obtained by reading 32,64,128,256,512,1024 blocks, respectively. With the increase of the number of blocks, the SNR was significantly improved. Aiming at the pulsar J0437-4715 baseband data recorded by the Medusa backend of the Parkes 64 m radio telescope, the problems of RFI and spectrum reversal in the data were analyzed. The algorithm was tested based on the data with bandwidth of 810–832 MHz, and the

pulse profile with SNR of about 255 was obtained. DSPSR was used to process Medusa data to obtain the 128 channels AR file, and PSRCHIVE was used to delete the 704-810 MHz frequency band to obtain the frequency phase map. By comparison, the pulse profile information processed by our algorithm is basically consistent with the results processed by DSPSR, and the phase is basically consistent with the results processed by DSPSR/PSRCHIVE.

Acknowledgments

This work is supported by National Key R&D Program of China Nos. 2021YFC2203502 and 2022YFF0711502; the National Natural Science Foundation of China (NSFC) (12173077 and 12003062); the Tianshan Innovation Team Plan of Xinjiang Uygur Autonomous Region (2022D14020); the Scientific Instrument Developing Project of the Chinese Academy of Sciences, Grant No. PTYQ2022YZZD01; the Operation, Maintenance and Upgrading Fund for Astronomical Telescopes and Facility Instruments, budgeted from the Ministry of Finance of China (MOF) and administrated by the Chinese Academy of Sciences (CAS); Natural Science Foundation of Xinjiang Uygur Autonomous Region (2022D01A360). Data resources are supported by China National Astronomical Data Center (NADC). This work is supported by Astronomical Big Data Joint Research Center, co-founded by National Astronomical Observatories, Chinese Academy of Sciences. The algorithms in this article have been applied Taurus High-Performance Computing Cluster of Xinjiang Astronomical Observatory, CAS, during the testing process.

References

Bassa, C. G., Pleunis, Z., & Hessels, J. W. T. 2017, A&C, 18, 40
De, K., & Gupta, Y. 2016, ExA, 41, 67
Ergesh, T., Li, J., Duan, X.-F., Pei, X., & Wen, Z.-G. 2022, RAA, 22, 025002
Hewish, A., Bell, S. J., Pilkington, J. D. H., Scott, P. F., & Collins, R. A. 1968, Natur, 217, 709
Hickish, J., Abdurashidova, Z., Ali, Z., et al. 2016, JAI, 5, 1641001
Hobbs, G., & Edwards, R. 2012, Tempo2: Pulsar Timing Package, Astrophysics Source Code Library, record, ascl:1210.015
Hobbs, G., Manchester, R. N., Dunning, A., et al. 2020, PASA, 37, e012
Kong, X., Zheng, X., Zhu, Y., Zhang, Q., & Huang, Y. 2021, in 8th IEEE Int. Conf. on Cyber Security and Cloud Computing (CSCloud)/2021 7th IEEE Int. Conf. on Edge Computing and Scalable Cloud (EdgeCom) (Washington, DC: IEEE), 103
Li, N. 2015, Research and design of high speed SAR ADC, Master's thesis, South East Univ.
Liu, W., Meng, Q., Wang, C., et al. 2022, PASA, 134, 015008
Lorimer, D. R., & Kramer, M. 2012, Handbook of Pulsar Astronomy (Cambridge: Cambridge Univ. Press)
Luo, J.-T., Chen, L., Han, J.-L., et al. 2017, RAA, 17, 9
Naldi, G., Bartolini, M., Mattana, A., et al. 2017, MEMSAI, 88, 206
Pennucci, T. T. 2015, Wideband Observations of Radio Pulsars, PhD thesis, Univ. of Virginia
Rickett, B. 1975, ApJ, 197, 185
Robishaw, T., & Heiles, C. 2021, in The WSPC Handbook of Astronomical Instrumentation, Volume 1: Radio Astronomic al Instrumentation, ed. A. Wolszczan, Vol. 127 (Singapore: World Scientific)
Stairs, I. H. 1998, Observations of Binary and Millisecond Pulsars with a Baseband Recording System, PhD thesis, Princeton Univ., New Jersey
van Straten, W., & Bailes, M. 2011, PASA, 28, 1
van Straten, W., Demorest, P., & Oslowski, S. 2012, AR&T, 9, 237